# Effect of nitrogen on generalized stacking fault energy and stacking fault widths in high nitrogen steels

S. Kibey [a], J.B. Liu [b], M.J. Curtis [b,c], D.D. Johnson [b,a], H. Sehitoglu [a,*]

[a] *Department of Mechanical and Industrial Engineering, University of Illinois, Urbana-Champaign, 1206, W. Green Street, Urbana, IL 61801, USA*
[b] *Department of Material Science and Engineering, University of Illinois, Urbana-Champaign, 1304, W. Green Street, Urbana, IL 61801, USA*
[c] *Franklin W. Olin College of Engineering, Olin Way, Needham, MA 02492, USA*

## Abstract

We use a generalized Peierls–Nabarro model fitted to generalized stacking fault energies (GSFE) calculated from ab initio density functional theory to study the effect of interstitial nitrogen content on stacking faults (SF) in {1 1 1} plane of face-centered cubic (fcc) Fe–N alloys. These simplified systems are reliable representatives of fcc Fe–Mn–N steels, for example, as Mn acts to stabilize fcc relative to body-center phase but hardly affects the GSFE. Here we study the dependence of stable SF widths of Fe–N alloys on GSFE versus percent nitrogen. In contrast to the classical Volterra solution, in which the SF width depends only on intrinsic SFE value, our results reveal a strong dependence of SF widths on intrinsic, unstable and maximally unstable SFE values. The model predicts finite SF widths for negative intrinsic SFE values, a result which cannot be explained by the Volterra model, but arises due to the finite (and positive) unstable SFE barrier that must be traversed even if the intrinsic SFE is negative, i.e. stable. This result has critical importance for the observed SF formation and maximum widths. Namely, the stacking fault width is found to depend non-monotonically on the percentage of nitrogen with a maximum critical shear stress at 1 wt.% (4 at.%) N, in agreement with experiment, and also suggests a non-monotonic critical shear stress dependence on nitrogen content.
© 2006 Acta Materialia Inc. Published by Elsevier Ltd. All rights reserved.

*Keywords:* Peierls model; Ab-initio electron theory; Dislocations; fcc steels; Modeling

## 1. Introduction

High nitrogen steels (HNS) have emerged as a promising class of materials because of their remarkably superior mechanical properties which are due to the addition of interstitial nitrogen. Nitrogen stabilizes austenite and its solubility in austenite is higher than carbon, resulting in higher toughness and improved strength [1]. The addition of interstitial nitrogen has been reported to increase significantly the flow stress of polycrystalline austenitic stainless steels [1–3]. Similar results have been reported in studies conducted on Hadfield steel single crystals [4,5] and austenitic stainless steel single crystals [4,6–8].

Nitrogen has been found also to affect the dislocation structure and deformation mechanisms, particularly twinning, in austenitic steels. Previous studies have shown an early activation of twinning in nitrogen-alloyed Hadfield steel single crystals [4,5]. This is attributed to the lowering of the intrinsic stacking fault energy (SFE) due to nitrogen addition, resulting in increased separation of partials required for twin nucleation. On the other hand, in austenitic stainless steels, planar dislocation structures are observed for low nitrogen contents (⩽0.4 wt.% N) and planar slip is the primary deformation mechanism [6,7]. In these alloys, twinning is suppressed in favor of planar slip for all orientations due to addition of nitrogen. The formation of coplanar arrays of dislocations and occurrence of planar slip has been attributed to short range order induced by nitrogen [9–11]. For higher nitrogen contents

---

($\geqslant 0.7$ wt.% N), extensive twinning is observed [12,13] in austenitic stainless steel single crystals. These studies indicate that the SFE of austenitic stainless steels depends non-monotonically on nitrogen content.

It is, thus, seen that the mechanical response and properties of HNS are intimately related to the effect of nitrogen and nitrogen content on the stacking fault energy, and perhaps the related short-range order. The impact of the addition of nitrogen on SFE (or, more generally, the SFE $\gamma$-surface) is, however, not yet clear. Several researchers have reported that addition of nitrogen results in a decrease in the SFE of austenitic steels [14,15]. In contrast to these experimental results, other studies have found that SFE increases with nitrogen content [16]. Finally, some studies have reported a nonmonotonic influence of nitrogen content on the SFE of austenitic steels [3,17,18]. Since, SFE governs the deformation mechanisms and stress–strain behavior of face-centered cubic (fcc) alloys, it is important to determine the effect of nitrogen content on the SFE of HNS. This issue is addressed in the present study.

A complete specification of SFE (or SF width) and its dependence on solute content requires a robust, yet convenient framework to describe extended dislocations spanning multiple length scales. At macroscopic scale, stacking faults and their interaction with dislocations are described within the framework of continuum elasticity usually incorporated in crystal plasticity models. However, continuum elasticity models cannot capture atomic-level entities like dislocation cores which are known to significantly influence the mechanical behavior of crystals. Hence, an accurate description of stacking faults (and various defects, in general) at microscopic scale requires atomistic models, since continuum elasticity breaks down at these length scales. The gap between microscopic and macroscopic approaches can be successfully bridged through the so-called mesoscale models, which incorporate features of both the continuum approach and atomistics.

Currently, two types of mesoscale approaches have been adopted by the research community: (i) The use of dislocation dynamics at mesoscale in conjunction with molecular dynamics (MD) at microscale. In this approach, short-range dislocation interactions are captured using MD, forming the basis of 'local rules' [19], which are subsequently integrated into mesoscale dislocation dynamics models [19,20]. (ii) The use of Peierls–Nabarro (P-N) model to describe dislocation cores and dislocation mobility in semiconductor materials [21] and fcc, body-centered cubic (bcc) and hexagonal close-packed (hcp) alloys [22].

In recent years, there has been considerable interest in the P-N model due to the advances in atomistic simulations facilitating an accurate computation of generalized stacking fault energies [21,23–28]. The generalized stacking fault energy (GSFE), first introduced by Vitek [29], is a comprehensive definition of stacking fault energy. In fcc alloys, a single layer intrinsic stacking fault is formed when the regular fcc stacking of the {1 1 1} planes is changed from $\ldots ABCABC \ldots$ to $\ldots ABCA|CABC \ldots$, where | indicates

the position of the fault. In general, an $n$-layer stacking fault is formed if this disruption in stacking is extended over $n$ layers. Here we focus on single-layer stacking faults. It is possible to generate a single-layer stacking fault on {1 1 1} planes in fcc alloys by shifting the upper half of the crystal relative to the lower half by a displacement vector $\boldsymbol{u}$ along the $\langle 1 1 2 \rangle$ direction. The fault energy $\gamma$ of different sheared lattice configurations can be computed as a function of displacement $\boldsymbol{u}$ (or its components $u_x$ and $u_z$), defined as $\gamma(\boldsymbol{u})$ or $\gamma(u_x, u_z)$. The function $\gamma(\boldsymbol{u})$, termed generalized stacking fault energy (GSFE) by Vitek [29], is represented as a surface ($\gamma$-surface) or a curve ($\gamma$-curve) along the $\langle 1 1 2 \rangle$ direction.

Fig. 1 shows the fault configurations of interest, formed during the shear of the fcc lattice along the $\langle 1 1 2 \rangle$ direction. The Burgers vector of the partial dislocation producing the shear is denoted by $\mathbf{b}_p = 1/6\langle 1 1 2 \rangle$. Fig. 2 shows the $\gamma$-curve associated with this shear along with the plan view of the fcc structure shown in Fig. 1. All fault energies are determined relative to the energy of the fcc structure. Shear displacement through $u_z = 0.5|\mathbf{b}_p|$ along the $\langle 1 1 2 \rangle$ direction results in the unstable fault structure shown in Fig. 1 having fault energy $\gamma_{us}$ (point u on the $\gamma$-curve in Fig. 2). The fault energy $\gamma_{us}$ was termed as the unstable SFE by Rice [30] and this terminology is followed throughout this paper. Of special interest here, is the stable fault structure formed due to a shear displacement $u_z = |\mathbf{b}_p|$ (see Fig. 1) corresponding to the local minimum s on the $\gamma$-curve with fault energy $\gamma_{isf}$ (see Fig. 2). The equilibrium fault structure corresponds to the intrinsic stacking fault (ISF) on {1 1 1} plane with $\gamma_{isf}$ as the intrinsic stacking fault energy (the intrinsic stacking fault energy has been also referred to the stable stacking fault energy by several researchers [31,32] and both terms are used interchangeably in this paper). Further shear beyond point s on the $\gamma$-curve along the $\langle 1 1 2 \rangle$ direction results in another unstable structure at $u_z = 2|\mathbf{b}_p|$ (Fig. 1). Due to the local, high energy, unstable $\ldots ABCAA \ldots$ stacking, this structure corresponds to a global maximum SFE, denoted by $\gamma_{max}$ here (point m on the $\gamma$-curve). It is noted that while both points u and m on the $\gamma$-curve in Fig. 2 correspond to unstable structures, the respective fault energies, the required shear displacements and stacking sequences are completely different. It is, therefore, necessary to determine both $\gamma_{us}$ and $\gamma_{max}$ in addition to the intrinsic SFE $\gamma_{isf}$ for a complete description of the $\gamma$-curve along the $\langle 1 1 2 \rangle$ direction.

The GSFE data, determined from ab initio electronic calculations, serves as an input to the continuum P-N model which can be utilized to determine several useful macro-parameters such as the Peierls stress, stacking fault widths, energy required for cross-slip etc. The P-N model, therefore, provides a convenient scheme to incorporate data from ab initio electronic calculations into continuum (crystal plasticity) models.

The classical P-N model [33,34] has several limitations, the most important being its limited applicability to narrow dislocations. The P-N model predicts very high elastic energies and unrealistic estimates of Peierls stress for narrow
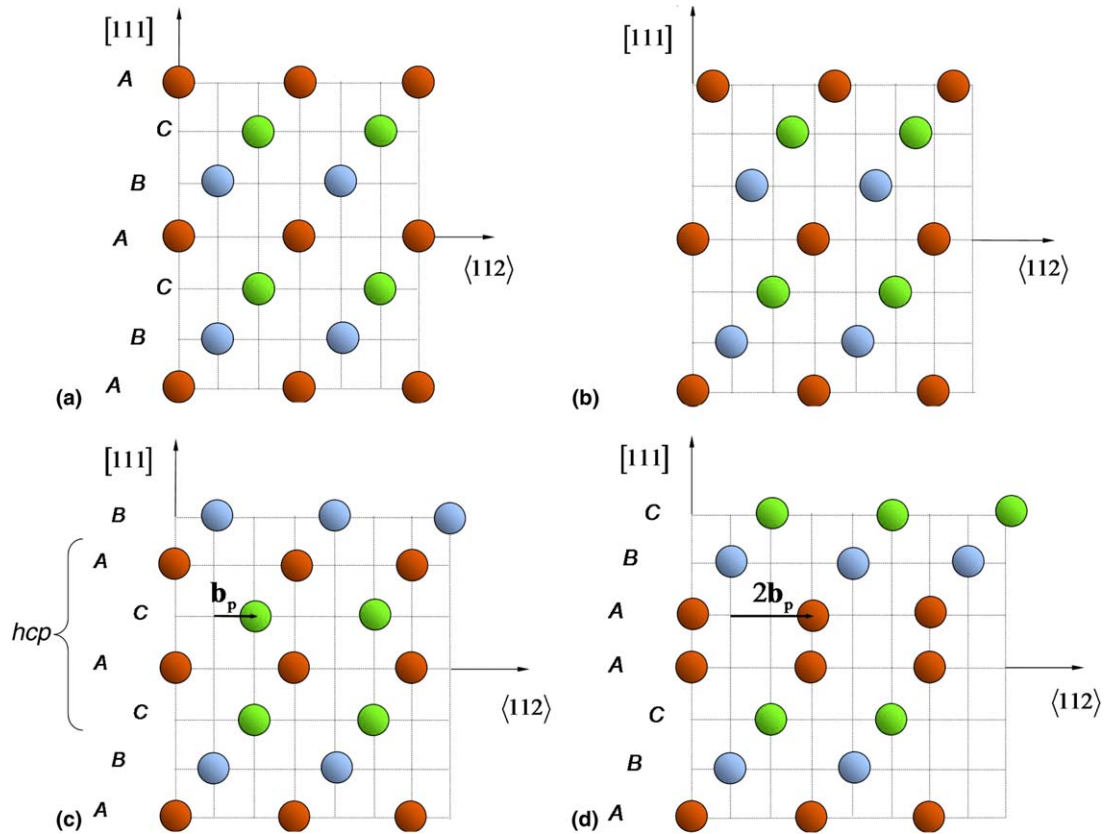
Fig. 1. Generation of generalized SFE curve (γ-curve) along the ⟨112⟩ direction. (a) fcc structure: point b on the γ-curve in Fig. 2. (b) Unstable fault structure: point u on the γ-curve in Fig. 2. (c) Stable intrinsic SF structure: point s on the γ-curve in Fig. 2. (d) Unstable fault structure: point m on the γ-curve in Fig. 2.
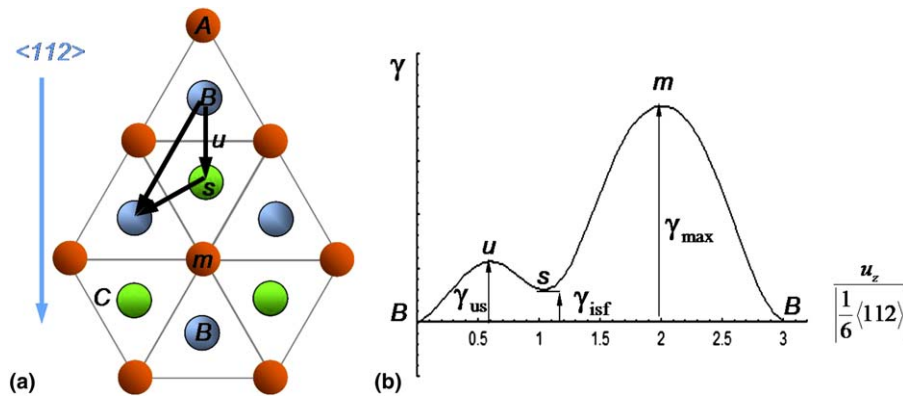


Fig. 2. FCC stacking and the γ-curve for an fcc alloy. Points u, s and m denote unstable, stable and maximum SFE points respectively. (a) Plan view of ...ABCABC... fcc stacking. (b) fcc GSFE curve generated by a shear of B layer relative to A layer along the ⟨112⟩ direction.

dislocation cores. Joos and Duesbery [25] modified the original P-N formalism and generalized it to narrow dislocation cores. Bulatov and Kaxiras [24] pointed out that P-N model uses two different expressions—one continuous and one discrete—for misfit energy to compute the slip distribution and Peierls stress, respectively. Further, the classical approach neglects transverse degrees of freedom during translations over Peierls barrier. To overcome these limitations, Bulatov and Kaxiras proposed a semi-discrete variational generalized Peierls–Nabarro model which removes these inconsistencies. Miller et al. [35] proposed

a nonlocal formulation of P-N model by accounting for the effect of large gradients in slip distributions through a nonlocal contribution to misfit energy. Lu et al. [36] investigated the effect of atomic relaxation on Peierls stress and found that atomic relaxation can lower the Peierls stress by an order of magnitude for narrow dislocations. Although all these investigations have served to overcome several limitations of Peierls–Nabarro model itself, there is a need to implement the P-N model in a consistent manner to couple atomistics with continuum models for prediction of materials behavior.

In this paper, we present a generalized Peierls–Nabarro model to describe extended dislocations and their stacking fault energies in fcc Fe–N alloys. The fcc Fe–N systems are a good representative of fcc Fe–Mn–N systems, as shown later by addressing directly substitutional disorder in Fe-Mn via electronic-structure calculations. By eliminating the complexity of substitutional disorder, we may simplify the system and focus on the critical factors related to the $\gamma$-surface, and, moreover, use band-structure methods requiring perfectly ordered unit cells that permit full relaxations of cell and internal atomic coordinates. The consideration of a more simple Fe–N binary alloy then allows us to illustrate the predictive capabilities of the generalized P-N model. The purpose of the present work is:

(1) to investigate the effect of nitrogen content in fcc alloys on the GSFE.
(2) to correlate the width of stable SF in fcc alloys with the GSFE.

The generalized stacking fault energy of Fe–N alloys has been computed by ab initio density functional theory (DFT). The effect of nitrogen content on GSFE is investigated by varying the N content in the alloy from 0 to 2.0 wt.% N (i.e., up to 8.0 at.% N). As will be seen, the stable stacking fault width is found to depend strongly on the nitrogen content and GSFE, in particular, the unstable SFE value. The generalized P-N model has been utilized in the past to explore the effect of maximum and stable SFE on the stacking fault width in a 'typical' isotropic fcc metal [37]. However, their results do not explicitly reveal the dependence of SF width on unstable SFE. Results of the present investigations show that unstable SFE energy value is a physically critical parameter determining the width of stacking faults in fcc alloys.

The outline of the paper is as follows. The dissociation of a perfect dislocation into partial dislocations in fcc alloys is briefly discussed in Section 2. The limitations of the classical Volterra model are also discussed and the need for a generalized Peierls–Nabarro model is highlighted. The generalized Peierls–Nabarro model for an extended edge dislocation and the associated ab initio DFT calculations are described in Section 3 and details on interstitial N as well as substitutional Mn and how chemical disorder impacts the SFE are provided. The GSFE results from ab initio DFT calculations are presented in Section 4. Stacking fault width predictions of P-N model based on these GSFE surfaces are also presented. The significance of these results is discussed in Section 5 and some key observations are made regarding the dependence of stable SF width on N content and $\gamma$-surface. We close in Section 6 with final remarks and a summary.

## 2. Background

As already noted, dislocations in fcc crystals prefer to exist in an energetically favorable configuration as planar
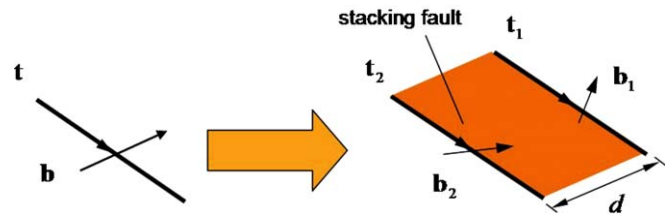


Fig. 3. Dissociation of a perfect dislocation into partial dislocations in an fcc lattice.

defects called intrinsic stacking faults (ISF) bound by two Shockley partial dislocations (Fig. 3). The dissociation in (1 1 1) plane can be expressed as

$$\mathbf{b} = \mathbf{b}_1 + \mathbf{b}_2$$
$$\tfrac{1}{2}[1\,\bar{1}\,0] = \tfrac{1}{6}[1\,\bar{2}\,1] + \tfrac{1}{6}[2\,\bar{1}\,\bar{1}] \tag{1}$$

The local stacking sequence inside the intrinsic stacking fault is hcp-like: $\ldots ACACA \ldots$ while the region outside the stacking fault retains its fcc stacking (Fig. 1). Within the framework of the classical Volterra model, the width $d$ of the stacking fault for a given extended dislocation depends only on the intrinsic stacking fault energy $\gamma_{isf}$ [38] and is given by

$$d = \left( \frac{\mu}{2\pi\gamma_{isf}} \right) \left[ (\mathbf{b}_1 \cdot \mathbf{t}_1)(\mathbf{b}_2 \cdot \mathbf{t}_2) + \frac{(\mathbf{b}_1 \times \mathbf{t}_1) \cdot (\mathbf{b}_2 \times \mathbf{t}_2)}{(1-\nu)} \right] \tag{2}$$

where $\mu$ is the shear modulus, $\nu$ is the Poisson's ratio and $\mathbf{t}_1$ and $\mathbf{t}_2$ are the line directions of the partial dislocations with Burgers vectors $\mathbf{b}_1$ and $\mathbf{b}_2$, respectively.

Clearly, Eq. (2) suggests no dependence of the stable stacking fault width $d$ on $\gamma$-surface except on the stable SFE $\gamma_{isf}$. Further, Eq. (2) is based on force balance; a more general basis for determining the width of the stacking fault will be the minimization of total energy of the extended dislocation. A natural outcome of total energy minimization of an extended dislocation is that the width of the stable stacking fault will depend on the entire $\gamma$-surface. Our interest, here, is in characterizing how the stable SF width depends on the $\gamma$-surface. In particular, we seek a relationship of the form

$$d = f(\gamma_{isf}, \gamma_{us}, \gamma_{max}) \tag{3}$$

where, $\gamma_{us}$ and $\gamma_{max}$ denote the unstable and the maximum stacking fault energy values, respectively. In this work, we have achieved this characterization through the generalized Peierls–Nabarro model, which will be discussed next.

## 3. Methodology

### 3.1. Generalized Peierls–Nabarro model

Fig. 4 shows an edge dislocation with Burgers vector $\mathbf{b}$ in the (1 1 1) glide plane. It dissociates into partials $\mathbf{b}_1$ and $\mathbf{b}_2$ as given by Eq. (1). The cartesian coordinate axes $XYZ$ are set up as shown with $XZ$ as the glide plane, $X$-axis along the $\mathbf{b}$ (direction $[1\,\bar{1}\,0]$), $Z$-axis along the direction $[\bar{1}\,\bar{1}\,2]$ perpendicular to $X$-axis and $Y$-axis along the glide plane
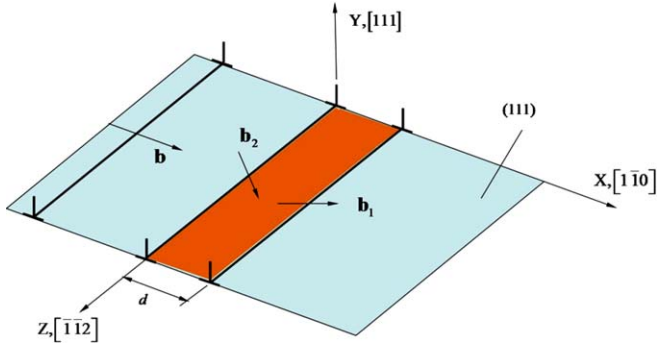
Fig. 4. Splitting of a perfect edge dislocation with Burgers vector **b** along the direction $[1\bar{1}0]$ on $(1\,1\,1)$ slip plane. The *XYZ* coordinate system is set up as shown.

normal $[1\,1\,1]$. The origin O of the *XYZ* coordinate system lies on the dislocation line of partial $\mathbf{b}_1$. Within the classical P-N framework, the displacement and shear stress for a pure edge dislocation lying at the origin O are given by

$$u_x(x) = -\frac{|\mathbf{b}|}{2\pi}\arctan\left(\frac{x}{w}\right)$$

$$\sigma_{xy}(x,0) = -\frac{\mu|\mathbf{b}|}{2\pi(1-v)}\frac{x}{x^2+w^2}$$

where, the core width $w$ is related to the separation $l$ between the two linear elastic half-spaces in the P-N model [38] as

$$w = \frac{l}{2(1-v)}$$

The classical P-N model can be generalized to the extended edge dislocation shown in Fig. 4. The partial dislocations have both edge and screw character. We denote the edge components of the Burgers vectors for the two partials as $\mathbf{b}_{e1}$ and $\mathbf{b}_{e2}$, respectively. The respective screw components are denoted as $\mathbf{b}_{s1}$ and $\mathbf{b}_{s2}$. The displacements and shear stresses due to edge and screw components can be written separately as follows:

For edge components:

$$u_x(x) = -\frac{1}{2\pi}\left[|\mathbf{b}_{e1}|\arctan\left(\frac{x}{w}\right) + |\mathbf{b}_{e2}|\arctan\left(\frac{x-d}{w}\right)\right] \text{ and}$$

$$\sigma_{xy}(x,0) = -\frac{\mu}{2\pi(1-v)}\left[\frac{|\mathbf{b}_{e1}|x}{x^2+w^2} + \frac{|\mathbf{b}_{e2}|(x-d)}{(x-d)^2+w^2}\right]$$

$$(4)$$

For screw components:

$$u_z(x) = -\frac{1}{2\pi}\left[|\mathbf{b}_{s1}|\arctan\left(\frac{x}{w}\right) + |\mathbf{b}_{s2}|\arctan\left(\frac{x-d}{w}\right)\right] \text{ and}$$

$$\sigma_{xy}(x,0) = -\frac{\mu}{2\pi}\left[\frac{|\mathbf{b}_{s1}|x}{x^2+w^2} + \frac{|\mathbf{b}_{s2}|(x-d)}{(x-d)^2+w^2}\right]$$

$$(5)$$

The total energy of the extended dislocation is given as the sum of elastic and misfit energy, of which the elastic energy can be determined from (4) and (5).

$$E_{\text{total}}(d) = E_{\text{elastic}}(d) + E_{\text{misfit}}(d)$$

where

$$E_{\text{elastic}}(d) = \int_{-r}^{r}(\sigma_{xy}u_x + \sigma_{yz}u_z)\,\mathrm{d}x \qquad (6)$$

and

$$E_{\text{misfit}}(d) = \int_{-r}^{r}\gamma(u_x,u_z)\,\mathrm{d}x \qquad (7)$$

Substituting from Eqs. (4) and (5) into Eq. (6), we have $E_{\text{elastic}}$ as a function of $d$:

$$\begin{aligned}
E_{\text{elastic}}(d) &= \frac{\mu}{4\pi}\left(\frac{|\mathbf{b}_{e1}^2|}{(1-v)} + |\mathbf{b}_{s1}^2|\right)\ln\left[\frac{r}{2w}\right] + \frac{\mu}{4\pi}\left(\frac{|\mathbf{b}_{e2}^2|}{(1-v)} + |\mathbf{b}_{s2}^2|\right) \\
&\quad \times \ln\left[\frac{r-d}{2w}\right] + \frac{\mu}{4\pi}\left(\frac{|\mathbf{b}_{e1}||\mathbf{b}_{e2}|}{(1-v)} + |\mathbf{b}_{s1}||\mathbf{b}_{s2}|\right) \\
&\quad \times \ln\left[1 + \frac{r^2}{w^2}\right]\arctan\left(\frac{r-d}{w}\right) \\
&\quad + \frac{\mu}{8\pi}\left(\frac{|\mathbf{b}_{e1}||\mathbf{b}_{e2}|}{(1-v)} + |\mathbf{b}_{s1}||\mathbf{b}_{s2}|\right)\ln\left[1 + \frac{(r-d)^2}{w^2}\right] \\
&\quad \times \arctan\left(\frac{r-d}{w}\right) + \frac{\mu}{8\pi}\left(\frac{|\mathbf{b}_{e1}||\mathbf{b}_{e2}|}{(1-v)} + |\mathbf{b}_{s1}||\mathbf{b}_{s2}|\right) \\
&\quad \times \ln\left[1 + \frac{(r+d)^2}{w^2}\right]\arctan\left(\frac{r+d}{w}\right)
\end{aligned} \qquad (8)$$

Note that in Eq. (8), the first two terms are the self-energy terms of the partial dislocations $\mathbf{b}_1$ and $\mathbf{b}_2$. The remaining terms are the interaction energy terms. Thus, the elastic contribution to the total energy is given by Eq. (8). However, as suggested by Eq. (7), the determination of misfit energy, $E_{\text{misfit}}$, requires an estimate of the $\gamma$-surface.

### 3.2. Ab initio calculation of γ-surfaces

In this work, the $\gamma$-surface has been determined for Fe–N using ab initio electronic-structure calculations based on DFT. The electronic structure calculations have been performed with a pseudopotential based plane-wave method, namely, the Vienna ab initio simulation package (VASP) [39–41], which gives accurate energy differences between lattice structures and allows for relaxations. VASP utilizes ultra-soft pseudopotentials (US-PP) as suggested by Vanderbilt [42] and supplied by Kresse and Hafner [43]. The local density exchange-correlation functional is a generalized gradient approximation (GGA) form based on non-local corrections [44,45]. All the GSFE results are using the US-PP, however, we validated with the more accurate VASP based on projected augmented wave (PAW) formalism [46]. For example, the fcc–hcp energy differences with US-PP and PAW are 68 and 69 meV per atom, respectively.

We have used $L$-layer $(1\,1\,1)$-based cell to calculate defect energies and performed shear along the $\langle 1\,1\,\bar{2}\rangle$ direction to create a single-layer intrinsic stacking fault defect (see Fig. 2), with adjacent faults being separated by $L = 3n$ atomic layers ($n$ is the number of fcc 3-layer $...ABC...$ stackings included). We assessed convergence

of the SFE with respect to increasing $L$, which indicates when the SF–SF interaction in adjacent cells due to periodic boundary conditions will become negligible. Initially, a defect-free $L$-layer (1 1 1) cell was fully relaxed (both unit cell vectors and internal atomic positions). This calculation was followed up by incorporating a defect and performing a full internal atomic relaxation, including perpendicular to the glide planes in defected cases, until the atomic forces were less than $\pm0.020$ eV/Å. Clearly, if the unit cell is large enough, the defect cannot affect the unit cell vectors, only the atoms adjacent to the defect. Regarding Brillouin zone integrations, the total energies were converged for 6-layer unit cells (for bcc and fcc primitive and hcp 2-atom cells) using a $12 \times 12 \times 12$ ($20 \times 20 \times 20$) special $k$-point mesh [47]. We used a 237.5 eV plane-wave energy cutoff. The energy cutoff and meshes provide the convergence of total energy to about 0.001 eV/cell. The fault energy values were found to be converged already for cells with 6 or more layers. Hence, all our calculations are based on a 6-layer-per-defect cell.

The need to investigate simplified binary Fe–N systems instead of the more complex Fe–Mn–N systems arises due to the necessity of using perfectly ordered cells to determine the $\gamma$-surface. We note that band-structure methods like VASP cannot address the effect of substitutional Mn and interstitial N disorder, as present in the processing of high-temperature fcc Fe–Mn–N HNS. To investigate the effect of substitutional and/or interstitial chemical disorder, we uses an all-electron, DFT total-energy method developed by Johnson et al. [48–50] based on the multiple-scattering method of Korringa, [51], Kohn and Rostoker [52] (KKR) combined with the coherent-potential approximation (CPA) [53,54]. This total-energy method within the CPA is widely and successfully used for dealing with chemical disorder and alloying effects. For KKR we use s-, p-, d-, and f-type orbitals in the basis, and von Barth and Hedin local density exchange-correlation [55]. We use a Gauss–Legendre quadrature contour integration with 24 energy points [56] to get self-consistent charges from the Green's function. For the various faults calculated we use the same 6-layer cell, Monkhorst–Pack $k$-point meshes, etc., as used for VASP. As the present KKR-CPA code uses the *atomic-sphere approximation* (ASA) to perform spatial integrals [57,58], it does not have local atomic forces, yet the KKR-ASA can provide reasonably accurate energy differences, often on par with full-potential results, as shown in Section 4.1. Thus, disorder can be included and we can accurately determine the effect of (in)homogeneous N distributions or the effects of homogeneous additions of Mn on the SFE. In Section 4.1 we demonstrate that the SFEs of Fe–Mn–N systems are not significantly affected by addition of Mn. This outcome allows us to focus only on representative Fe–N binaries.

Another important consideration in the perfectly ordered 6-layer (1 1 1) cells is the location of nitrogen atom relative to the single-layer hcp-type stacking fault. In our calculations, the N atoms were placed one, two and three

layers below the stacking fault at octahedral sites (the lowest energy sites). Our results indicate a strong dependence of stable stacking fault energy on the relative location of nitrogen atoms and this issue is discussed in detail in Section 4.2, along with comparison to the KKR-CPA results that provide direct determination of the SFE for homogeneous distribution of nitrogen.

Due to 60° angular symmetry of the fcc lattice in {1 1 1} slip planes, the GSFE surface has a 60° angular symmetry as well. Hence, only a sufficient number of points need to be calculated via DFT along the $\langle 1 1 2 \rangle$ and $\langle 1 1 0 \rangle$ directions to specify completely the $\gamma$-surface. A two-dimensional Fourier series has been fit through the electronically computed points in the (1 1 1) plane to estimate the GSFE. The Fourier series approximation is of the form

$$\gamma(u_x, u_z) \approx A_0 + A_1 \cos\left(\frac{4\pi u_x}{b}\right) + A_2 \cos\left(\frac{2\pi u_x}{b}\right) \cos\left(\frac{2u_z}{h}\right)$$
$$+ A_3 \cos\left(\frac{2\pi u_x}{b}\right) \sin\left(\frac{2u_z}{h}\right) + A_4 \cos\left(\frac{4u_z}{h}\right)$$
$$+ A_4 \cos\left(\frac{4u_z}{h}\right) + A_5 \cos\left(\frac{6u_z}{h}\right) + A_6 \cos\left(\frac{8u_z}{h}\right)$$
$$+ A_7 \sin\left(\frac{4u_z}{h}\right) \tag{9}$$

The above Fourier series approximation enables us to compute the misfit energy from Eq. (7). Computing both elastic and misfit energies, the total energy Eq. (6) can be minimized with respect to stacking fault width $d$. The $d$ at which the total energy of the extended dislocation is minimum will be the stable stacking fault width. The above minimization was carried out in Mathematica and the following equation was numerically solved for $d$ to obtain the stable stacking fault width:

$$\frac{\partial E_{\text{elastic}}(d)}{\partial d} = -\frac{\partial E_{\text{misfit}}(d)}{\partial d} \tag{10}$$

The above computations were carried out for different nitrogen contents corresponding to different values of stable and unstable SFE, and the width $d$ was determined. The results are summarized in the following section.

## 4. Results

### 4.1. Effects of substitutional Mn and interstitial N disorder on SFE

Fig. 5 show the calculated SFE for intrinsic and twin faults in fcc Fe–12Mn–$x$N (at.%) (a typical composition in Fe–Mn–N high nitrogen steels) versus the N content, with N in octahedral sites (which are lower in energy than the tetrahedral sites). Clearly, for homogeneous nitrogen distributions, each SFE approaches zero around 4–5 at.% N. As will be seen in Section 4.2, this zero value at 4–5 at.% N is the same as determined from the 'average' $\gamma$-curve obtained by averaging VASP $\gamma$-curves with N in different planes relative to the SF. The 'average' VASP $\gamma_{\text{isf}}$ values are listed in the first row of Table 1. Note that the
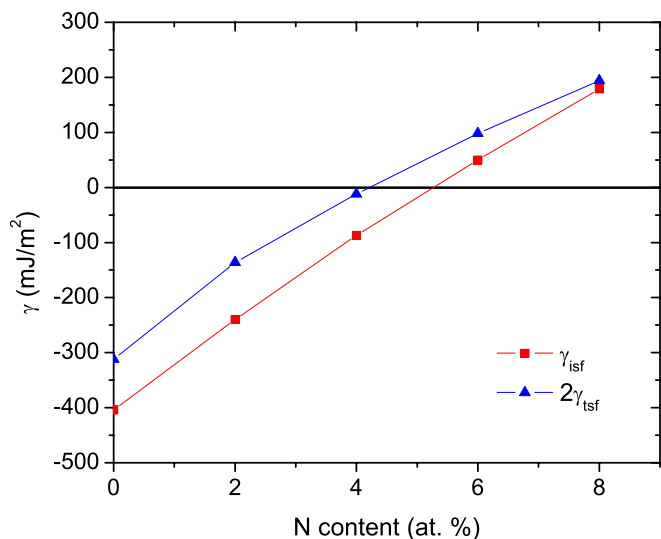
Fig. 5. KKR-CPA predictions of SFE in fcc Fe–12at.%Mn (mJ/m²) versus N (at.%) in octahedral sites for (squares) intrinsic and (triangles) twin faults, i.e., $2\gamma_{tsf}$. Ref. [59] shows why $\gamma_{isf} \neq 2\gamma_{tsf}$. For homogeneous N distributions, SFE are zero around 4–5 at.% N, as also found from the 'average' $\gamma$-curve from VASP, see text and Table 1.

Table 1
Fe–Mn–N stacking fault energies (in mJ/m²) versus N and Mn content (at.%) from KKR-CPA and 'averaged' VASP calculations, see text

| N content in Fe–$x$N | 0 | 4 | 8 | SFE/at.% |
|---|---|---|---|---|
| 'average' VASP $\gamma_{isf}$ | −380 | 0 | 200 | 73 |
| N content in Fe–12Mn–$x$N | 0 | 4 | 8 | 73 |
| KKR-CPA $\gamma_{isf}$ | −404 | −87 | 179 | |
| Mn content in Fe–$x$Mn | 0 | 6 | 12 | −3 |
| KKR-CPA $\gamma_{sf}^{est}$ | −393 | −411 | −429 | |

KKR-ASA and VASP agree well for pure Fe, −393 vs. −380 mJ/m², respectively.
Mn content hardly affects the SFE as shown in the final row from a KKR-CPA SFE estimated via $\gamma_{sf}^{est} \approx 2E^{hcp-fcc}/A_{111}$, where $A_{111}$ is the (111) planar area per atom. The last column shows the change in SFE per at.% impurity, highlighting the importance of N, not Mn, for affecting the SFE.
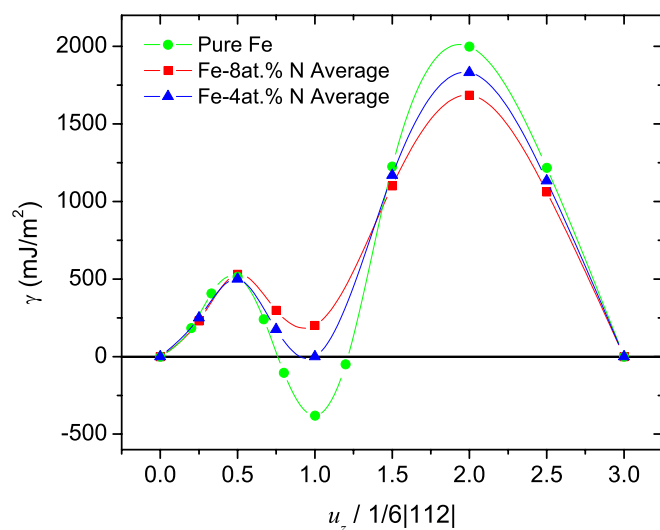


Fig. 6. $\gamma$-curves along the $\langle 112 \rangle$ direction for nitrogen contents of 0, 4.0 at.%N (1.0 wt.% N) and 8.0 at.%N (2.0 wt.% N) from VASP. See text for definition of 'average'.

VASP result is in agreement with the KKR-CPA result for pure Fe. According to Table 1, our KKR-CPA results show that Mn additions hardly alter the SFE (−3 mJ/m² per at.% Mn), whereas VASP and KKR-CPA show that N additions change the SFE by 73 mJ/m² per at.% N. We, therefore, conclude that the SFE of Fe–Mn–N is not dramatically affected by the addition of Mn, only by the addition of N. This result indicates that the fcc Fe–N systems are a good representative of fcc Fe–Mn–N systems. Hence, all the subsequent results discussed below pertain to a simplified fcc Fe–N binary alloy instead of Fe–Mn–N systems.

### 4.2. Effect of interstitial nitrogen on GSFE

Fig. 6 shows the DFT results of GSFE $\gamma$-curves along the $\langle 112 \rangle$ direction for an fcc Fe–N binary with varying nitrogen content. Two nitrogen contents were chosen to illustrate the effect of addition of interstitial nitrogen to fcc iron: 1.0 wt.% N (4.0 at.% N) and 2.0 wt.% N (8.0 at.% N). The 'average' $\gamma$-curves in Fig. 6 for 4 at.% N and 8 at.% N represent values corresponding to homogeneously distributed interstitial nitrogen, and are obtained by averaging the VASP results for different locations of N atoms relative to the SF. Again these 'average' values correlate well with the KKR-CPA results for disordered Fe–Mn–N alloy at around 4–5 at.% N (Table 1).

First, we note that the stable SFE for pure fcc iron is negative at −380 mJ/m². This implies that the hcp phase is energetically more favorable than the fcc phase for pure iron (indeed, for pure Fe, bcc is energetically the ground-state, followed by hcp then fcc phases). In other words, fcc iron would prefer to be in hcp configuration, if it can overcome the energy barrier $\gamma_{us}$, either by thermal activa-

tion or externally applied stress. Addition of 1 wt.% N (4.0 at.% N) resulted in a significant increase in the stable stacking fault energy value from −380 to 0 mJ/m², while the maximum unstable SFE value changed from 2000 to 1830 mJ/m². The corresponding changes in unstable SFE values were found to be insignificant. A stable stacking fault energy of 0 mJ/m² for Fe–4 at.%N indicates that addition of 1 wt.% N made both fcc and hcp configurations equally stable. With addition of 2 wt.% N (8 at.% N), the stable SFE value increased to about 200 mJ/m². Again, the unstable SFE value was not observed to change significantly. The maximum unstable SFE value, however, decreased to 1690 mJ/m². It is, thus, clear from Fig. 6 that addition of interstitial N significantly increases the stable SFE of iron and decreases the maximum SFE. For the representative fcc Fe–N systems considered here, the stable SFE is negative for N content less than 1.0 wt.%, zero at exactly 1.0 wt.% N (i.e. at 4 at.%) and positive for N content exceeding 1.0 wt.%.

In order to determine the effect of generalized stacking fault energy on stable stacking fault width, the $\gamma$-surfaces

corresponding to the DFT derived $\gamma$-curves shown in Fig. 6 were approximated by a Fourier series fit of the form given by Eq. (9). Fig. 7 shows a representative $\gamma$-surface fit corresponding to Fe–4.0 at.%N (Fe–1.0 wt.%N).

Fig. 8 shows the stacking fault widths predicted by the Peierls–Nabarro model as a function of the $\gamma_{isf}$ (and therefore, interstitial N content). The stable SFE $\gamma_{isf}$ was varied from $-380$ mJ/m$^2$ (corresponding to pure Fe) to 400 mJ/m$^2$ (corresponding to N content $>2$ wt.%) and the stable stacking fault width $d$ was determined for each case by solving Eq. (10) using Mathematica. The classical Volterra solution (Eq. (2)) is also plotted for comparison. It is seen that, while the Volterra solution predicts finite stacking fault widths only for $\gamma_{isf} > 0$ and diverges to infinity as $\gamma_{isf}$ approaches zero, the Peierls–Nabarro model predicts finite stacking fault widths even when $\gamma_{isf} \leqslant 0$. This result suggests that the stable stacking fault width is not governed by $\gamma_{isf}$ alone. It will be shown below that stacking fault width depends on unstable SFE and maximum SFE as well and physically based arguments will be provided supporting this conclusion. From Fig. 8, it is further noted that the width of the stacking fault increases with increase in $\gamma_{isf}$ from $-380$ mJ/m$^2$ and reaches a peak, finite value at 0 mJ/m$^2$ (corresponding to 1.0 wt.% N) suggesting a nonmonotonic dependence of yield strength on nitrogen content.

We now investigate the dependence of stacking fault width on unstable and maximum SFE in the spirit of Eq. (3). Fig. 9 shows variation of stable stacking fault width with unstable SFE, $\gamma_{us}$, for constant $\gamma_{isf}$ and $\gamma_{max}$ corresponding to 1.0 wt.% N. The $\gamma_{us}$ value for Fe–1.0 wt.%N from DFT calculations is 514 mJ/m$^2$ (see Fig. 6). In Fig. 9, $\gamma_{us}$ was decreased in steps from 514 to 50 mJ/m$^2$ keeping all other SFE values constant. It is clear from Fig. 9 that stacking fault width $d$ increases from $5|\mathbf{b}|$ to about $8.4|\mathbf{b}|$ with decrease in $\gamma_{us}$. This can be explained as follows: a decrease in $\gamma_{us}$ results in a lowering of energy
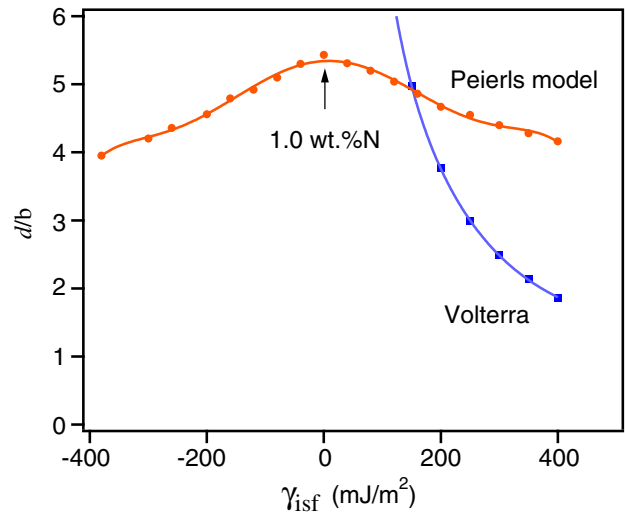


Fig. 8. Variation of SF width with stable intrinsic SFE, with maximum and unstable SFE kept constant. The Peierls model predicts a finite SF width for $\gamma_{isf} \leqslant 0$, while the Volterra solution is defined only for $\gamma_{isf} > 0$, see text. Maximum SF width is for $\gamma_{isf} = 0$ at 1.0 wt.% N.

barrier to be overcome by the partials in order to transition from the fcc to hcp configuration. With a reduction in the energy barrier, it is easier for the partials to attain hcp configuration by overcoming $\gamma_{us}$, resulting in a wider stacking fault. Alternatively, the higher the barrier for the partials, the more difficult it will be for the partials to overcome the barrier and attain the energetically favorable hcp configuration. Hence, the extended dislocation will have a reduced SF width with increase in $\gamma_{us}$.

Fig. 10 reveals the effect of variation in maximum SFE, $\gamma_{max}$, in addition to $\gamma_{us}$. Here, both $\gamma_{max}$ and $\gamma_{us}$ are varied but the ratio $\gamma_{max}/\gamma_{us}$ is kept constant at 4.0. The stable stacking fault energy, $\gamma_{isf}$, which corresponds to the composition Fe–1.0 wt.%N, is kept constant. It is seen from the plot that the stacking fault width increases from
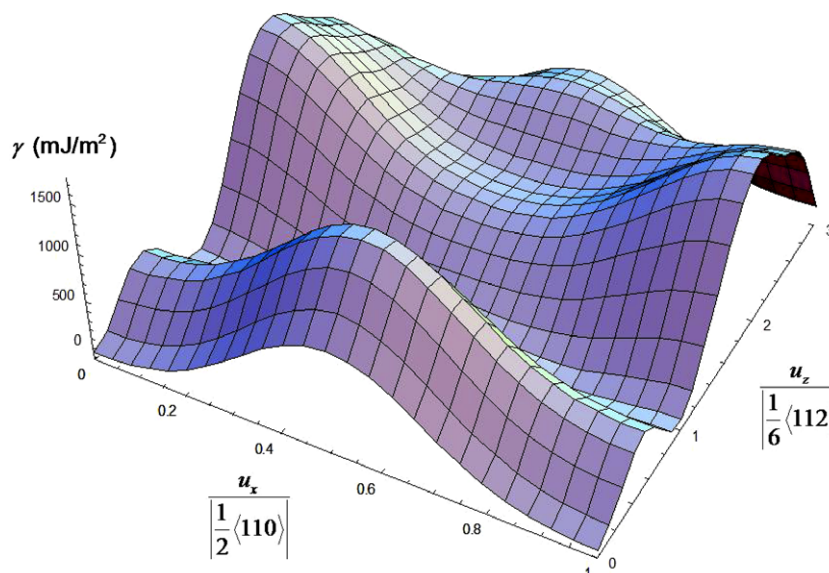


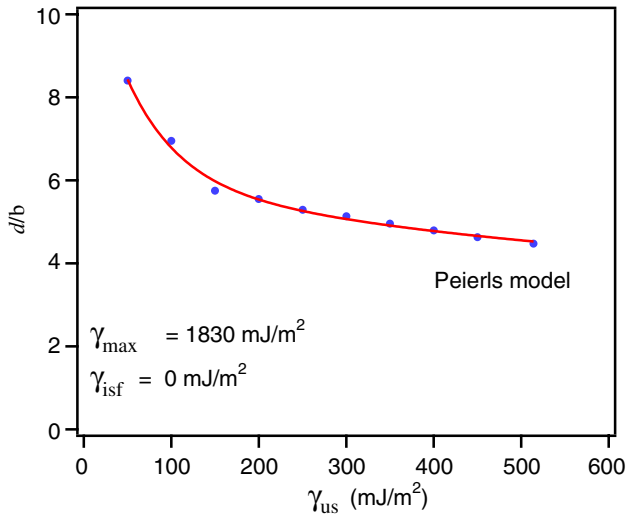Fig. 7. Fourier series fit for $\gamma$-surface of fcc Fe–4.0at.%N. $\gamma_{isf}$ is zero for this case.

Fig. 9. Variation of SF width with unstable SFE. Maximum and stable SFE values are kept constant. An increase in $\gamma_{us}$ raises the barrier to be overcome by the partials, resulting in a narrower stacking fault.
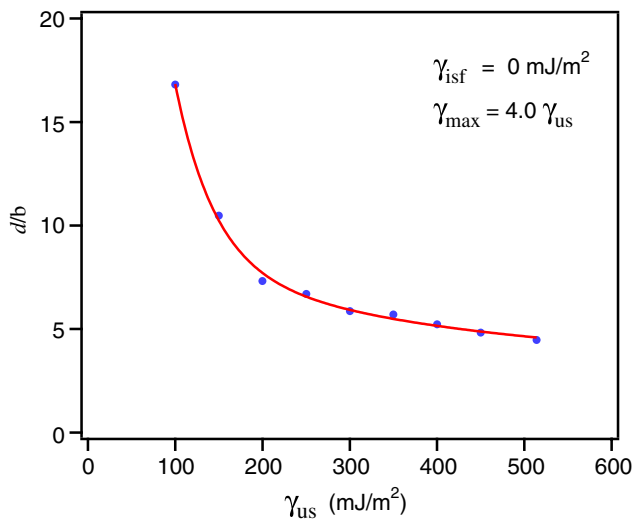


Fig. 10. Stable SF width versus unstable SFE for constant ratio of $\gamma_{max}/\gamma_{us}$.

$5|\mathbf{b}|$ to about $15|\mathbf{b}|$ corresponding to a decrease in $\gamma_{us}$ from 514 to 100 mJ/m$^2$. A comparison with Fig. 9 shows that the effect of variation of both unstable and maximum SFE is more pronounced than $\gamma_{us}$ alone. Physically, it is difficult to motivate the dependence of $d$ on $\gamma_{max}$, because the partial dislocations do not need to overcome the barrier due to $\gamma_{max}$ during zig-zag shear along the $\langle 112 \rangle$ slip directions. It is, however, possible that variation in $\gamma_{max}$ changes the profile of the $\gamma$-surface in a way as to make it easier for the partials to overcome the $\gamma_{us}$ barrier and attain the hcp configuration.

Finally, within the 6-layer (111) cell used here, we explored the effect of the location of nitrogen atom relative to the single-layer stacking fault on the $\langle 112 \rangle$ $\gamma$-surface. So far, in the above results, we have used average $\gamma$ values corresponding to disordered fcc lattices with homogeneously distributed interstitial nitrogen. To deter-

mine whether nitrogen atoms have an affinity for the hcp stacking fault, the N atoms were placed at the stacking fault as well as one layer, two layers and three layers below stacking fault at the octahedral sites. Fig. 11 shows the variation in the $\gamma$-surface along the $\langle 112 \rangle$ direction for Fe–8.0 at.%N. The stable SFE is found to be highest when the N atom is at the stacking fault and it decreases as the N atom is placed progressively further away from the single-layer stacking fault. The stacking fault energy is found to be the least when the N atom is three layers away (i.e. half-way between the periodic array of single-layer stacking faults) from the hcp stacking fault. A similar trend is noted for Fe–4 at.%N (see Fig. 12). Clearly, it is energetically favorable for N atom to be as far as possible from the stacking fault. However, there will be
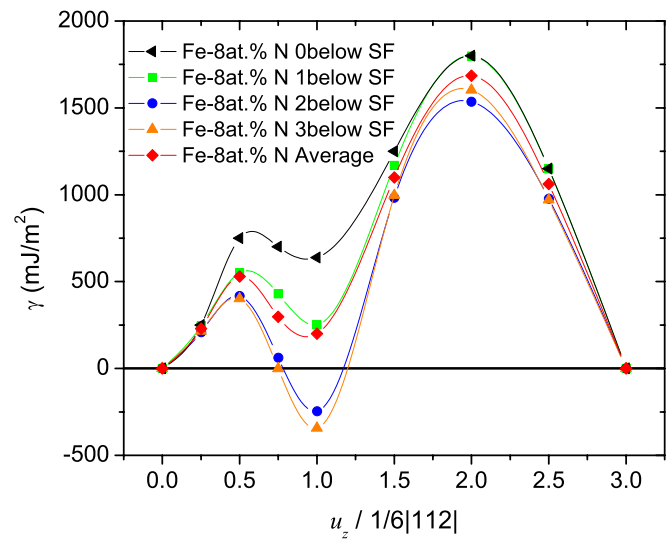


Fig. 11. Change of $\gamma$-curve along the $\langle 112 \rangle$ due to location of nitrogen atom relative to the SF for Fe-8 at.%N (2.0 wt.% N). Average curve gives a positive stable SFE.
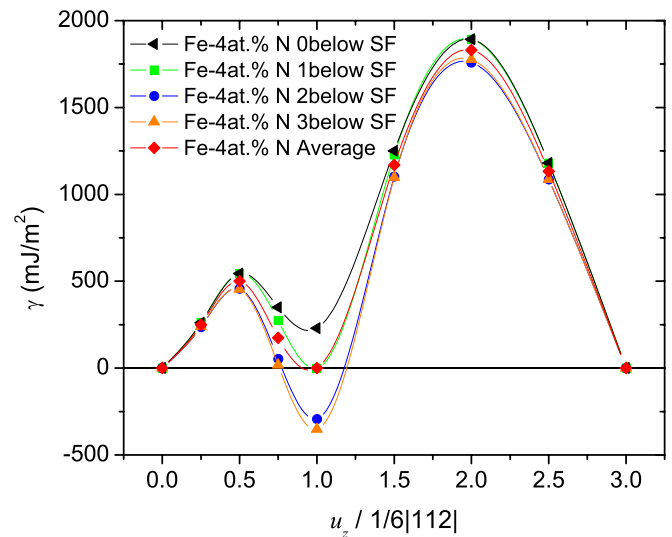


Fig. 12. Change of $\gamma$-curve along the $\langle 112 \rangle$ due to nitrogen atom location relative to the SF for Fe-4 at.%N (1.0 wt.% N). Average curve gives a zero energy stable SFE.

a distribution due to processing, kinetics, as well as interactions with dislocations, etc.

Figs. 11 and 12 also reveal that the DFT stable stacking fault energy strongly depends on the position of nitrogen atoms in the atomistic model. The 'average' $\gamma$-curve, corresponding to 'homogeneously distributed' nitrogen, have been reproduced from Fig. 6 and included in Figs. 11 and 12 for comparison. The 'average' $\gamma$-curves are seen to lie approximately in the middle of the position-dependent curves. This 'average' $\gamma$-surface is representative of homogeneously distributed N, as concluded by comparing to independent KKR-CPA calculations with perfectly random occupations of N in the octahedral interstitial sites, both, with and without Mn substitutional impurities.

## 5. Discussion

In this paper, we have demonstrated a methodology for design of high-nitrogen steels which spans multiple length scales. The Peierls–Nabarro model has been implemented in a consistent manner to couple atomistics based upon density-functional theory with continuum models for prediction of mechanical behavior of high-nitrogen steels. The predictions of the generalized P-N model have been found to be consistent with experimental observations and provide insight into the mechanisms governing the deformation behavior of high nitrogen steels.

We have shown that addition of Mn hardly affects the SFE of in Fe–Mn–N steels. In fact, our KKR-CPA calculations of SFE for fcc Fe–$x$N (Table 1) show that substitutional Mn alters the SFE very little (about $-3$ mJ/m$^2$ per at.% Mn). On the other hand, N content has a pronounced effect on SFE of Fe–Mn–N steels (about 75 mJ/m$^2$ per at.% N), as seen in Table 1.

Our DFT results indicate an increase in stable SFE with increase in nitrogen content, up to 1.0 wt.% N), see Fig. 6. Notably, our results show that nitrogen stabilizes the fcc phase (austenite) relative to hcp phase, such that, at 4.0 at.% N (i.e., 1.0 wt.% N), fcc and hcp are degenerate in energy. Therefore, addition of nitrogen makes the fcc stacking in high-nitrogen steels energetically more favorable relative to hcp stacking. Hence, the high-nitrogen steels will prefer to stay in the more energetically favorable austenitic state. In other words, nitrogen serves to stabilize austenite. This result is in excellent agreement with the experimentally reported property of nitrogen as an austenitic stabilizer [1].

Our SF width results shown in Figs. 8–10 reveal that the stable stacking fault width is not a function of $\gamma_{isf}$ alone, as suggested by the Volterra model. Instead, the stacking fault width is found to depend on the entire $\gamma$-surface, specifically, on $\gamma_{us}$ and $\gamma_{max}$ in addition to $\gamma_{isf}$. It is seen that formation of the stacking fault requires the leading partial to overcome the energy barrier represented by $\gamma_{us}$. Consequently, our model predicts that finite width stacking faults can be formed in fcc alloys with zero or negative stable stacking fault energies due to positive energy barrier $\gamma_{us}$. The dependence of stacking fault width on GSFE has been reported before [37]; however, previous studies have not revealed a clear dependence of SF width on unstable SFE. We have identified $\gamma_{us}$ as a physically critical parameter determining the width of a stable stacking fault in fcc alloys.

The stacking fault width was found to depend non-monotonically on the interstitial nitrogen content in the Fe–N binary alloy (see Fig. 8). Cross-slip of extended screw dislocations in high nitrogen steel crystals will require resolved shear stress sufficient for the recombination of partials. For crystal orientations where cross-slip of screw dislocations is the dominant deformation mechanism, Fig. 8 suggests that the contribution to critical stress for recombination of partials at the onset of cross-slip will initially increase with nitrogen content up to 1.0 wt.% and then decrease with further addition of nitrogen beyond 1.0 wt.%. To the authors' knowledge, experimental studies on dependence of critical shear stress on N content up to and beyond 1.0 wt.% in Fe–Mn–N steels have not been reported so far, but, similar trends of non-monotonic dependence have been experimentally observed and reported for yield stress of polycrystalline high nitrogen steels [60]. Our results are in agreement with these experimental investigations. This suggests that the model is able to predict strain hardening of HNS due to nitrogen. Finally, Fig. 8 also indicates that increasing N content up to 1.0 wt.% will make cross-slip of screw dislocations more difficult due to increasing SF width, suggesting that an alternate deformation mechanism like twinning must be activated to accommodate plastic deformation, as is experimentally observed in HNS [1].

## 6. Conclusion

We have employed first-principles, density-functional theory (DFT) electronic-structure methods to calculate the (1 1 1) plane generalized stacking fault energy surface for fcc Fe and fcc Fe–N alloys as a function of nitrogen content. We have demonstrated that addition of substitutional Mn does not significantly affect the SFE of Fe–Mn–N steels, while interstitial N does and that the binary fcc Fe–N systems are good representatives of the more complex fcc Fe–Mn–N systems. Utilizing a generalized Peierls–Nabarro model, the stable stacking fault widths were correlated to the DFT generalized stacking fault energies. Our investigations show that the width of stacking faults in fcc alloys is determined by the complete $\gamma$-surface, not just by the stable SFE, $\gamma_{isf}$. Specifically, our results reveal that unstable SFE energy value, $\gamma_{us}$, is a physically critical parameter governing the stacking fault width, rather than the stable SFE, for example. Due to the effect of $\gamma_{us}$, finite stacking fault widths were predicted by the generalized Peierls–Nabarro model for zero or negative stable stacking fault energies, for which the classical Volterra solution is not valid. The stable stacking fault width was also found to depend strongly on interstitial nitrogen content. The

stacking fault width, and consequently, the critical stress for the onset of cross-slip of screw dislocations, was found to depend non-monotonically on the interstitial nitrogen content in the fcc Fe–N system. This trend is in agreement with the experimentally observed trends for yield stress dependence of fcc alloys on nitrogen content. Finally, our results suggest that an increase in N content up to 1.0 wt.% will likely promote an alternate mechanism like twinning instead of cross-slip to accommodate plastic deformation, which is consistent with experimental observations.

## Acknowledgements

## References

[1] Gavriljuk G, Berns H. High nitrogen steels. 1st ed. Berlin: Springer-Verlag; 1999.
[2] Reed RP. JOM 1989;41:16.
[3] Gavriljuk VG, Berns H, Glavatskaya N, Sozinov A, Petrov YN. Mater Sci Eng A 1999;271:14.
[4] Chumlyakov YI, Kireeva I, Sehitoglu H, Litvinova E, Zaharova E, Luzginova N. Mater Sci Forum 1999;318:395.
[5] Canadinc D, Karaman I, Sehitoglu H, Chumlyakov YI, Maier HJ. Metall Mater Trans A 2003;34A:1821.
[6] Karaman I, Sehitoglu H, Maier HJ, Chumlyakov YI. Acta Mater 2001;49:3919.
[7] Kireeva I, Chumlyakov Y, Luzginova N. Phys Met Metallogr 2002;94:508.
[8] Kireeva IV, Luzginova NV, Chumlyakov YI, Karaman I, Lichter BD. J Phys IV 2004;115:223.
[9] Byrnes MLG, Grujicic M, Owen WS. Acta Metall 1987;35:1853.
[10] Sassen J, Garrett-Reed AJ, Owen WS. In: Proceedings of high nitrogen steels–HNS 88; 1988. p. 159.
[11] Thomas G. Acta Metall 1963;11:1369.
[12] Chumlyakov YI, Korotaev AD. Russ Phys J 1992;35:3.
[13] Chumlyakov YI, Korotaev AD. Phys Met Metallogr 1994;78:153.
[14] Schramm RE, Reed RP. Metall Trans A 1975;6:1345.
[15] Stoltz RE, Vander Sande JB. Metall Trans A 1980;11:1033.
[16] Petrov YN. Kiev: Naukova Dumka; 1978. p. 262.
[17] Fujikura M, Takada K, Ishida K. ISIJ Int 1975;15:464.
[18] Yakubtsov IA, Ariapour A, Perovic DD. Acta Mater 1999;47: 1271.
[19] Devincre B, Kubin LP. Mater Sci Eng A 1997;234:8.
[20] Bulatov V, Abraham FF, Kubin L, Devincre B, Yip S. Nature 1998;391:669.
[21] Joos B, Ren Q, Duesbery MS. Phys Rev B 1994;50:5890.
[22] Vitek V. Prog Mater Sci 1992;36:1.
[23] Juan YM, Kaxiras E. Philos Mag A 1996;74:1367.
[24] Bulatov VV, Kaxiras E. Phys Rev Lett 1997;78:4221.
[25] Joos B, Duesbery MS. Phys Rev Lett 1997;78:266.
[26] Hartford J, von Sydow B, Wahnstrom G, Lundqvist BI. Phys Rev B 1998;58:2487.
[27] Lu G, Kioussis N, Bulatov VV, Kaxiras E. Phys Rev B 2000;62:3099.
[28] Lu G, Bulatov VV, Kioussis N. Phys Rev B 2002;66:1441031.
[29] Vitek V. Philos Mag 1968;18:773.
[30] Rice JR. J Mech Phys Sol 1992;40:239.
[31] Mehl MJ, Papaconstantopolous DA, Kioussis N, Herbranson M. Phys Rev B 2000;61:4894.
[32] Van Swygenhoven H, Derlet PM, Frøseth AG. Nat Mater 2004;3:399.
[33] Peierls R. Proc Phys Soc Lond 1940;52:34.
[34] Nabarro FR. Proc Phys Soc Lond 1947;59:256.
[35] Miller R, Phillips R, Beltz G, Ortiz M. J Mech Phys Sol 1998;46:1845.
[36] Lu G, Kioussis N, Bulatov VV, Kaxiras E. Philos Mag Lett 2000;80:675.
[37] Schoeck G. Phil Mag A 1999;79:1207.
[38] Hirth JP, Lothe J. Theory of dislocations. 2nd ed. New York (NY): Wiley Interscience; 1982.
[39] Kresse G, Hafner J. Phys Rev B 1993;47:558.
[40] Kresse G, Furthmuller J. Phys Rev B 1996;54:11169.
[41] Kresse G, Furthmuller J. Comput Mater Sci 1996;6:15.
[42] Vanderbilt D. Phys Rev B 1990;41:7892.
[43] Kresse G, Hafner J. J Phys 1994;6:8245.
[44] Perdew J, Zunger A. Phys Rev B 1981;23:5048.
[45] Perdew J, Wang Y. Phys Rev B 1992;45:13244.
[46] Kresse G, Joubert D. Phys Rev B 1999;59:1758.
[47] Monkhorst HJ, Pack JD. Phys Rev B 1976;13:5188.
[48] Johnson DD, Nicholson DM, Pinski FJ, Gyorffy BL, Stocks GM. Phys Rev Lett 1986;56:2088.
[49] Johnson DD, Nicholson DM, Pinski FJ, Stocks GM, Gyorffy BL. Phys Rev B 1990;41:9701.
[50] Johnson DD, Pinski FJ. Phys Rev B 1993;48:11553.
[51] Korringa J. J Phys 1947;13:392.
[52] Kohn W, Rostoker N. Phys Rev 1954;94:1111.
[53] Soven P. Phys Rev 1967;156:809.
[54] Taylor DW. Phys Rev 1967;156:1017.
[55] von Barth U, Hedin LJ. J Phys C 1979;5:1629.
[56] Johnson DD, Pinski FJ, Stocks GM. Phys Rev B 1984;30: 5508.
[57] Andersen OK. Phys Rev B 1984;12:3060.
[58] Phariseau P, Temmerman WM. The electronic structure of complex systems. New York (NY): Plenum Press; 1984.
[59] Finkenstadt D, Johnson DD. Phys Rev B 2006;73:024101.
[60] Rawers J, Slavens G. J Mater Eng Perform 1995;4:697.